marine drugs

Article

Activity-Guided Discovery and Functional Characterization of VTPPHVE, a Tyrosinase-Inhibitory Peptide from Golden Pompano (*Trachinotus anak*) Muscle Proteins

Nan An, Yanting Zeng, Hong Wang *, Weidong Bai, Hao Dong, Jinming Peng, Yujuan Xu and Jun Li *

College of Light Industry and Food Technology, Zhongkai University of Agriculture and Engineering, Guangzhou 510225, China; joeyan077@163.com (N.A.); 13427688868@163.com (Y.Z.); whitebai2001@163.com (W.B.); donghao@zhku.edu.cn (H.D.); pengjmiyz@163.com (J.P.); xuyujuan@gdaas.cn (Y.X.)
* Correspondence: whongaq@163.com (H.W.); lijun@zhku.edu.cn (J.L.)

Abstract

Marine-derived bioactive peptides are promising natural enzyme inhibitors, but their functional robustness and inhibition behavior require experimental validation. Golden pompano (*Trachinotus anak*) muscle proteins were subjected to ultrasound-assisted neutral protease–papain hydrolysis, activity-guided ultrafiltration, LC–MS/MS identification, and synthetic-peptide validation. The <3 kDa ultrafiltration fraction showed the highest activity (75.43% tyrosinase inhibition and 51.40% apparent Cu^{2+} chelation) and was selected for LC–MS/MS. Five candidate peptides were synthesized after stepwise prioritization. VTPPHVE showed the lowest IC_{50} value for tyrosinase inhibition (113.41 μM) and exhibited the strongest apparent Cu^{2+}-chelating activity among the synthesized peptides (141.54 μM). VTPPHVE retained comparable inhibitory activity after pH 2–10 treatment and heating at 20–100 °C, and showed detectable apparent activity after simulated gastrointestinal treatments, although the digested samples were not normalized to an equivalent peptide concentration at the assay stage and digestion-fluid blanks were not included. Enzyme kinetics indicated mixed-type inhibition, with a concentration-dependent decrease in apparent Vmax and an increase in apparent Km. Molecular docking placed VTPPHVE in an interchain surface region spanning H-subunit chains A and B, while a 100 ns molecular dynamics simulation supported the dynamic persistence of the docking-derived model after initial conformational adjustment. These results identify VTPPHVE as a marine fish-derived tyrosinase-inhibitory peptide and extend its characterization from sequence-level discovery to functional activity retention, enzyme kinetics, and exploratory structural modeling.

Keywords: golden pompano; tyrosinase inhibitor; bioactive peptide; enzyme kinetics; molecular docking; molecular dynamics

Check for updates

Academic Editor: Tatiana V. Ovchinnikova

Received: 22 September 2026
Revised: 21 October 2026
Accepted: 26 October 2026
Published: 28 October 2026

Copyright: © 2026 by the authors. Licensee MDPI, Basel, Switzerland. This article is an open access article distributed under the terms and conditions of the Creative Commons Attribution (CC BY) license.

1. Introduction

Tyrosinase (EC 1.14.18.1) is a dinuclear copper-containing oxidoreductase that plays a critical role in melanin biosynthesis and represents an important molecular target in pigmentation-related research. By catalyzing the hydroxylation of L-tyrosine to L-3,4-dihydroxyphenylalanine (L-DOPA) and the subsequent oxidation of L-DOPA to dopaquinone, tyrosinase initiates the enzymatic cascade responsible for melanin formation [1,2]. Excessive melanin accumulation is closely associated with hyperpigmentation-related disorders and has therefore stimulated extensive research into safe and effective

tyrosinase inhibitors for pharmaceutical and cosmeceutical applications [1]. In addition to its biological relevance, tyrosinase-mediated oxidation also contributes to enzymatic browning in food systems, further expanding the practical significance of tyrosinase inhibitors [3,4]. Although kojic acid is widely used as a reference inhibitor in tyrosinase-related studies, limitations associated with stability and application-dependent performance have encouraged the exploration of alternative inhibitors from natural sources [5,6].

Marine-derived bioactive peptides have attracted increasing attention as promising natural compounds because of their structural diversity, biological activities, and potential applications in pharmaceutical, nutraceutical, and cosmeceutical fields. Compared with conventional small-molecule inhibitors, peptide-based bioactive compounds may exhibit advantages including high sequence specificity, structural tunability, and favorable biocompatibility [7]. Numerous marine-derived peptides have been reported to possess tyrosinase-inhibitory activity, with proposed mechanisms involving interaction with substrate-access regions, modulation of residues surrounding the catalytic pocket, and coordination with catalytic copper ions [8,9]. In particular, marine protein-derived peptides represent valuable candidates for tyrosinase inhibition because marine organisms provide abundant protein resources containing diverse amino acid sequences that can generate biologically active peptide fragments after enzymatic hydrolysis [7,8]. Recent studies have demonstrated that peptide-based tyrosinase inhibitors from marine or food protein sources can exhibit inhibitory activities through combined effects of molecular recognition, metal-chelating ability, and antioxidant properties [9,10].

Marine fish proteins, in particular, are valuable peptide precursors due to their abundance, nutritional quality, and diverse amino acid composition. Enzymatic hydrolysis of marine-derived proteins has been widely employed to release functional peptides with various biological activities, including antioxidant, antihypertensive, and enzyme-inhibitory effects [11]. Golden pompano (*Trachinotus anak*) is a commercially important marine fish species with considerable potential as a source of functional peptides [12]. Previous studies have identified bioactive peptides from golden pompano proteins with enzyme-inhibitory activities [11,13,14], highlighting its value as an underexplored marine peptide resource. However, tyrosinase-inhibitory peptides derived from golden pompano muscle proteins and their molecular mechanisms remain largely unexplored.

In this study, golden pompano (*T. anak*) muscle proteins were used to establish an activity-guided workflow comprising protease screening, ultrasound-assisted dual-enzyme hydrolysis, ultrafiltration, LC–MS/MS identification, stepwise candidate prioritization, peptide synthesis, and in vitro validation. The functional activity retention of the synthesized peptides was evaluated after pH, thermal, and simulated gastrointestinal treatments. The lead peptide VTPPHVE was further characterized by enzyme inhibition kinetics, exploratory molecular docking, and a 100 ns molecular dynamics simulation. The study aimed to identify a marine fish-derived tyrosinase-inhibitory peptide with experimentally validated activity, characterize its response to processing- and digestion-related conditions, define its kinetic inhibition pattern, and evaluate the structural plausibility of a docking-derived peptide–tyrosinase interaction model.

2. Results and Discussion

2.1. Protease Screening and Dual-Enzyme Ratio Optimization

The hydrolytic efficiencies of six commercial proteases were first compared using DH and SPC as evaluation indicators. Papain and neutral protease showed higher DH values than alkaline protease, bromelain, Flavourzyme, and trypsin. Papain produced the highest DH, while neutral protease showed a comparable value (Figure 1A). Both enzymes also generated relatively high SPC. Compared with trypsin, papain increased

DH and SPC by approximately 28.4% and 49.8%, respectively, whereas neutral protease increased these values by approximately 24.5% and 48.0%, respectively. Therefore, papain and neutral protease were selected to construct a dual-enzyme hydrolysis system. At this preliminary screening stage, DH and SPC were used to assess hydrolysis efficiency and peptide solubilization. Tyrosinase inhibition was subsequently used as the functional response for optimization of the hydrolysis conditions. The neutral protease-to-papain ratio significantly affected hydrolysis efficiency (Figure 1B). Among the tested ratios, the 2:1 ratio produced the highest DH and SPC. Compared with papain alone, the 2:1 dual-enzyme system increased DH and SPC by approximately 9.6% and 6.6%, respectively. Compared with the 3:1 ratio, the 2:1 ratio improved these values by approximately 24.0% and 21.5%, respectively.

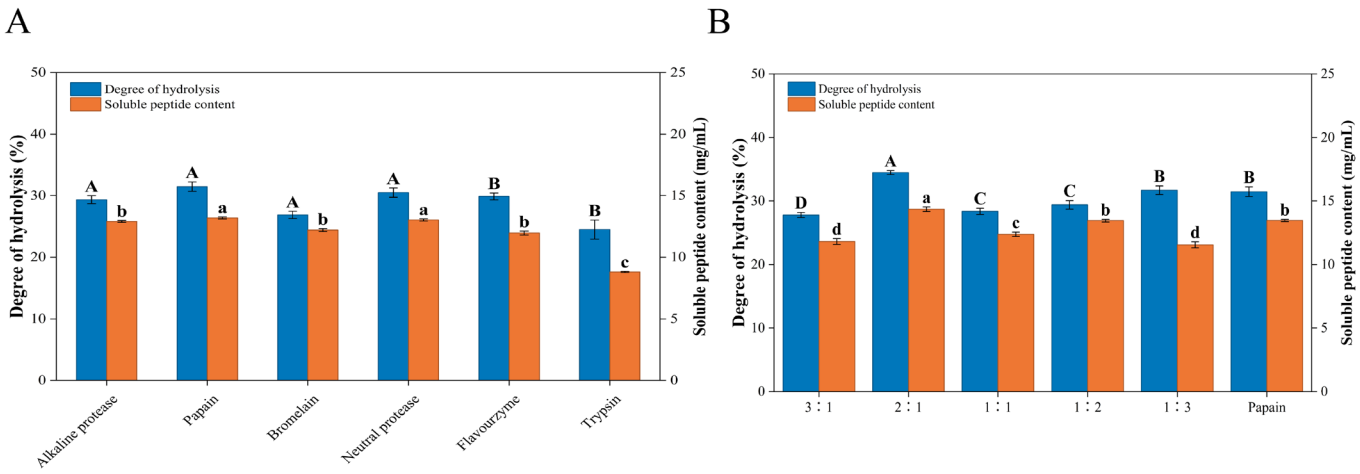


Figure 1. Screening of commercial proteases and optimization of the neutral protease-to-papain ratio based on hydrolysis performance. (**A**) Degree of hydrolysis and soluble peptide content of golden pompano muscle hydrolysates prepared with six commercial proteases. (**B**) Effects of different neutral protease-to-papain mass ratios and papain alone on degree of hydrolysis and soluble peptide content. Different uppercase and lowercase letters indicate significant differences in degree of hydrolysis and soluble peptide content, respectively ($p < 0.05$). Data are expressed as mean ± SD ($n = 3$).

The higher DH and SPC of the 2:1 system may reflect complementary cleavage by neutral protease and papain, allowing access to different peptide bonds. Because enzyme-specific cleavage sites and structural changes were not directly examined, the ratio was selected primarily from the measured DH and SPC.

2.2. Single-Factor Evaluation of Ultrasound-Assisted Dual-Enzyme Hydrolysis

2.2.1. Effects of Solid-to-Liquid Ratio and Enzyme Dosage

The solid-to-liquid ratio affected both tyrosinase inhibition and SPC (Figure 2A). The 1:4 (w/v) treatment produced the highest inhibition rate (approximately 63.91%) and SPC (17.73 mg/mL). Increasing the liquid proportion from 1:4 to 1:8 progressively reduced both responses. Under a fixed enzyme dosage per gram of muscle, excessive dilution may decrease productive enzyme–substrate encounters and lower the concentration of released active components [15]. A ratio of 1:4 was therefore used in subsequent experiments.

Tyrosinase inhibition increased as the total enzyme dosage rose from 600 to 1000 U/g substrate and then declined at 1200 and 1400 U/g (Figure 2B). The lower activity at the highest dosages, despite a relatively high SPC, indicates that soluble material concentration alone did not determine inhibition; extensive cleavage may have altered active sequences [16]. Dosages of 800, 1000, and 1200 U/g were selected for response surface optimization.

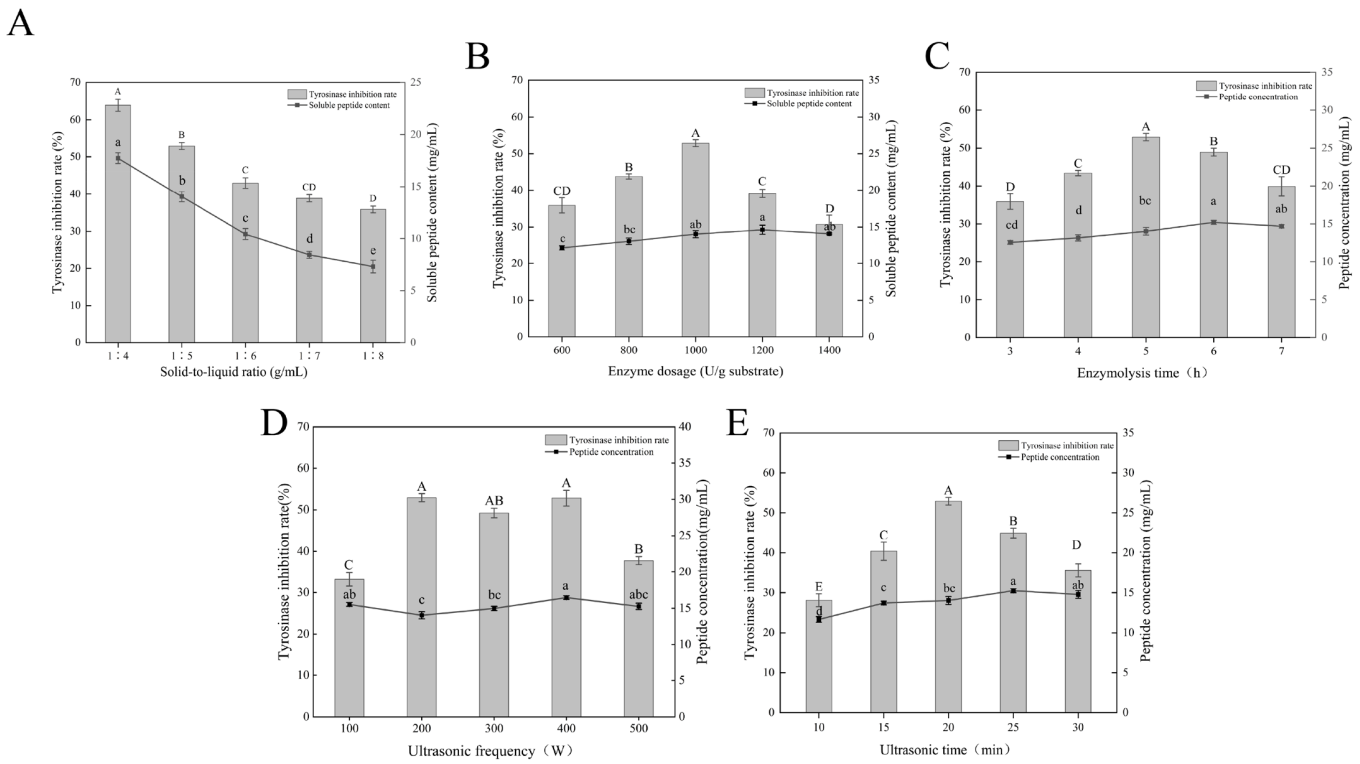


Figure 2. Effects of solid-to-liquid ratio (**A**), combined enzyme dosage (**B**), enzymatic hydrolysis time (**C**), ultrasonic power (**D**), and ultrasonic time (**E**) on tyrosinase inhibition and soluble peptide concentration. Different uppercase and lowercase letters within each panel indicate significant differences among treatment levels in tyrosinase inhibition and soluble peptide concentration, respectively ($p < 0.05$). Data are expressed as mean ± SD ($n = 3$).

2.2.2. Effect of Enzymatic Hydrolysis Time

Enzymatic hydrolysis time significantly influenced the formation of tyrosinase-inhibitory peptides (Figure 2C). The inhibition rate increased from 3 to 5 h, with the 5 h treatment showing an approximately 47.3% higher inhibition rate than the 3 h treatment. However, further prolonging the hydrolysis time to 6 and 7 h reduced the inhibitory activity, although the SPC remained relatively high. This result suggests that prolonged hydrolysis may have modified the peptide profile or further cleaved active sequences [13]. Thus, 4–6 h was selected for response surface optimization.

2.2.3. Effects of Ultrasonic Power and Ultrasonic Time

Ultrasonic power showed a nonlinear effect on the generation of tyrosinase-inhibitory peptides (Figure 2D). Increasing the ultrasonic power from 100 to 200 W enhanced the tyrosinase inhibition rate by approximately 59.5%, indicating that moderate ultrasonic power promoted the release of active peptides. A comparable inhibition rate was observed at 400 W; however, further increasing the power to 500 W reduced the inhibition rate by approximately 28.6% compared with 200 W. This decrease may be associated with excessive cavitation, localized heating, or structural disruption of active peptide fragments under overly intense ultrasound treatment [17]. Considering both inhibitory activity and energy input, 200 W was selected as the ultrasonic power for subsequent experiments.

Tyrosinase inhibition increased as ultrasonic time rose from 10 to 20 min and declined thereafter (Figure 2E). The highest activity occurred at 20 min, whereas SPC remained high at 25 min, again showing that activity was not determined solely by soluble material concentration. Ultrasonic time of 15–25 min was selected for optimization.

2.3. Response Surface Optimization and Experimental Validation

Enzyme dosage (A), enzymatic hydrolysis time (B), and ultrasonic time (C) were optimized using a Box–Behnken design, with tyrosinase inhibition rate as the response. The design matrix is shown in Table S3 and the ANOVA is summarized in Table S4. The fitted coded-factor equation was

$$Y = 71.48 + 1.38A + 3.10B - 0.07C + 1.26AB + 9.70AC - 2.56BC - 5.04A^2 - 10.36B^2 - 10.32C^2$$

where Y is the tyrosinase inhibition rate (%), and A, B, and C represent the coded values of enzyme dosage, enzymatic hydrolysis time, and ultrasonic time, respectively.

The model was significant ($p < 0.0001$), with a non-significant lack of fit ($p = 0.1699$) and an adjusted R^2 of 0.9828. Enzyme dosage and hydrolysis time had significant linear effects, whereas ultrasonic time did not. Significant AC and BC interactions and all quadratic terms indicated an optimal processing region, consistent with Figure 3.

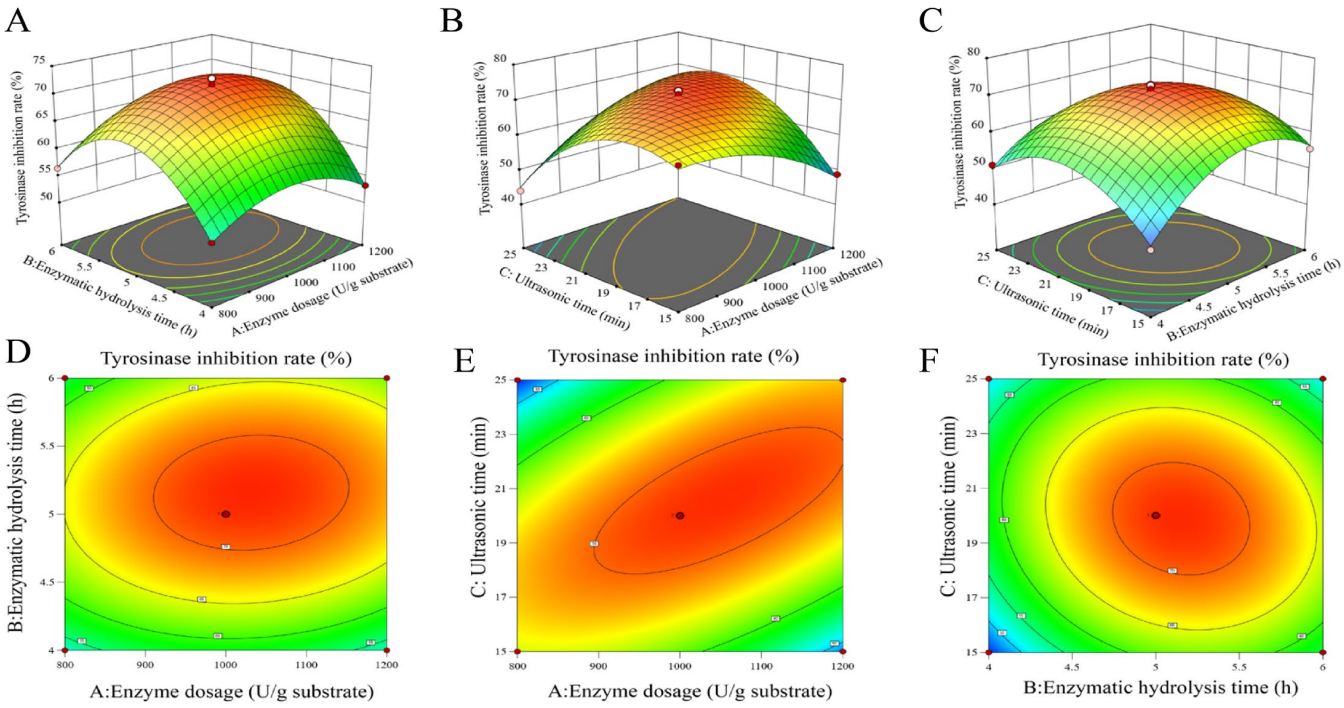


Figure 3. Response surface plots (**A**–**C**) and corresponding contour plots (**D**–**F**) showing the interactive effects of the selected process variables on tyrosinase inhibition. (**A**,**D**) Interaction between enzyme dosage and enzymatic hydrolysis time; (**B**,**E**) interaction between enzyme dosage and ultrasonic time; (**C**,**F**) interaction between enzymatic hydrolysis time and ultrasonic time.

The predicted optimal conditions were an enzyme dosage of 1049.39 U/g substrate, an enzymatic hydrolysis time of 5.15 h, and an ultrasonic time of 20.47 min. For practical operation, these values were adjusted to 1050 U/g substrate, 5.2 h, and 21 min. Under these conditions, the predicted inhibition rate was 71.89%, and the experimentally verified value was 69.17 ± 0.46%, corresponding to a relative error of 3.78%. Therefore, the optimized ultrasound-assisted dual-enzyme hydrolysis conditions were used for subsequent preparation and activity-guided fractionation.

2.4. Bioactivities of Hydrolysates from Different Treatments

To determine whether the optimized ultrasound-assisted process provided an advantage beyond ultrasound or enzymatic hydrolysis alone, the optimized ultrasound-assisted

enzymatic hydrolysis (UAE) hydrolysate was compared with the untreated, ultrasound-treated (US), and enzymatic hydrolysis (EN) samples at the same sample concentration (Figure 4A,B). UAE produced the highest tyrosinase-inhibitory, apparent Cu^{2+}-chelating, and ABTS radical-scavenging activities ($p < 0.05$). EN was more active than US, indicating that proteolytic cleavage was the principal contributor to the release of active components. The additional increase obtained with UAE is consistent with ultrasound-enhanced dispersion and enzyme accessibility.

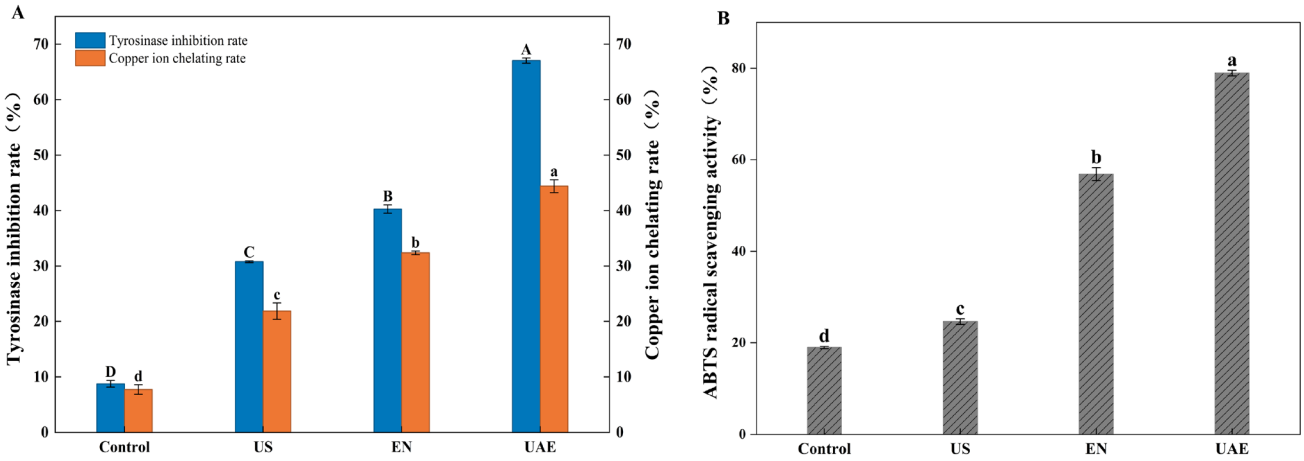


Figure 4. Effects of different processing treatments on the in vitro bioactivities of golden pompano muscle hydrolysates. (**A**) Tyrosinase inhibition and apparent Cu^{2+}-chelating activity; (**B**) ABTS radical-scavenging activity. Control, untreated sample; US, ultrasound-treated sample; EN, enzymatic-hydrolysis sample; UAE, ultrasound-assisted enzymatic-hydrolysis sample. Different uppercase and lowercase letters in panel A indicate significant differences among treatments in tyrosinase inhibition and apparent Cu^{2+}-chelating activity, respectively; different lowercase letters in panel B indicate significant differences in ABTS radical-scavenging activity ($p < 0.05$). Data are expressed as mean ± SD ($n = 3$).

The parallel increase in apparent Cu^{2+}-chelating activity and tyrosinase inhibition suggests that Cu^{2+}-chelating ability may be one of the contributing factors to the observed activity of the UAE hydrolysate because tyrosinase contains a binuclear copper center [8]. However, chelation cannot be treated as the sole mechanism; peptide–enzyme contacts, steric effects, and antioxidant properties may also contribute [9]. UAE was therefore selected for subsequent ultrafiltration and peptide identification.

2.5. Activity-Guided Ultrafiltration and Amino Acid Composition of Molecular Weight Fractions

2.5.1. Tyrosinase-Inhibitory and Apparent Cu^{2+}-Chelating Activities of Ultrafiltration Fractions

Ultrafiltration separated the optimized ultrasound-assisted enzymatic hydrolysate into >10, 5–10, 3–5, and <3 kDa fractions. At equal dry-mass concentration, the <3 kDa fraction showed the highest tyrosinase-inhibitory and apparent Cu^{2+}-chelating activities, reaching 75.43% and 51.40%, followed by the 3–5, 5–10, and >10 kDa fractions (Figure 5). Both activities were significantly higher than those of all other fractions ($p < 0.05$). Relative to the >10 kDa fraction, they increased by 14.60 and 16.91 percentage points, respectively.

The stronger activity of lower-molecular-weight fractions may reflect greater exposure of terminal groups and side chains involved in hydrogen bonding, electrostatic interactions, and metal coordination, together with reduced steric hindrance. However, this explanation remains tentative because each fraction contained complex peptide mixtures.

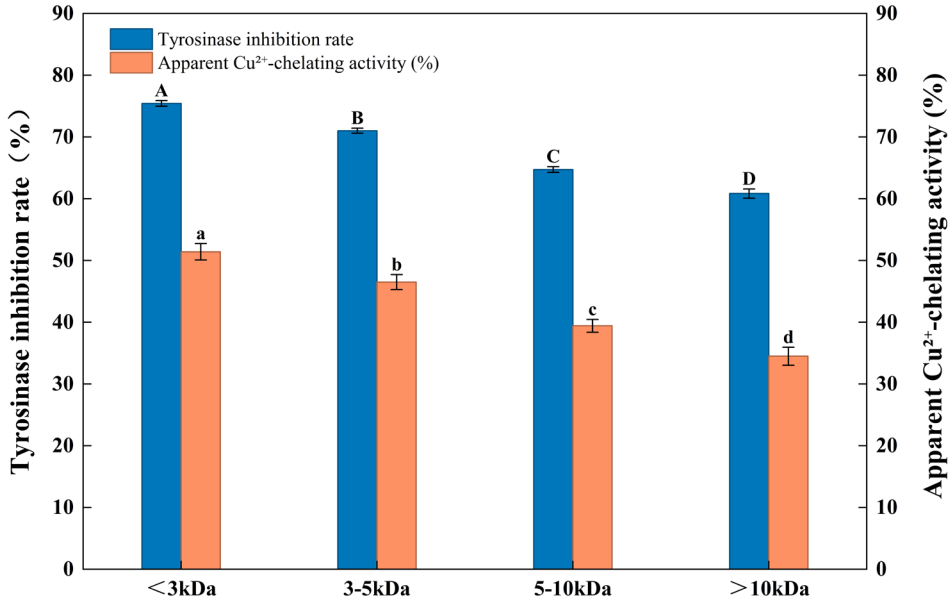


Figure 5. Tyrosinase-inhibitory and apparent Cu^{2+}-chelating activities of molecular weight fractions obtained from the optimized golden pompano muscle hydrolysate. Different uppercase and lowercase letters indicate significant differences among fractions in tyrosinase inhibition and apparent Cu^{2+}-chelating activity, respectively ($p < 0.05$). Data are expressed as mean ± SD ($n = 3$).

Based on its superior tyrosinase-inhibitory and apparent Cu^{2+}-chelating activities, the <3 kDa fraction was selected for subsequent LC–MS/MS analysis. Its acid-hydrolyzable amino acid composition was examined to provide compositional context for the observed activity.

2.5.2. Amino Acid Profiles of Molecular-Weight Fractions

The acid-hydrolyzable amino acid profiles differed among molecular weight fractions (Table S5). The <3 kDa fraction showed the strongest tyrosinase-inhibitory and apparent Cu^{2+}-chelating activities, indicating that total amino acid content was not the primary determinant of activity. The <3 kDa fraction contained higher levels of Phe, Pro, Leu, aromatic amino acids, and hydrophobic amino acids, which may favor hydrophobic or π-related interactions with tyrosinase [7,9]. Accessible carboxyl, amino, hydroxyl, and imidazole groups may also contribute to Cu^{2+} chelation [18]. Thus, the stronger activity of the <3 kDa fraction may be associated with its amino acid profile and the greater accessibility of functional groups in small peptides.

2.6. LC–MS/MS Identification and Stepwise Prioritization of Candidate Peptides

LC–MS/MS identified 4912 peptide sequences in the <3 kDa fraction. The identified sequences were first filtered according to peptide length (≤10 residues), predicted safety, and PEAKS identification confidence (−10lgP > 20), yielding 376 candidate sequences for further evaluation. These candidates were subsequently screened for favorable water solubility, resulting in 43 peptides that were subjected to molecular docking analysis. Based on the docking results, the ten peptides with the most favorable binding energies were shortlisted for further prioritization (Table 1). TIPred scores were then used as target-specific auxiliary information to support the prioritization of these shortlisted candidates rather than as a predefined exclusion criterion or a quantitative measure of inhibitory potency. Among the ten shortlisted peptides, five candidates, namely EEGSPDWRR, TPGPTGPIK, VTPPHVE, LDKPGPPT, and EKLGDLYR, were selected for chemical synthesis and subsequent experimental validation. These peptides had lengths of 7–9 residues and molecular

masses ranging from 777.97 to 1131.28 Da, and all were predicted to be non-toxic (Table 1). The annotated MS/MS spectra and identification metrics of the five synthesized peptides are provided in Figure S1 and Table S8, respectively. No fixed numerical weights were assigned to the individual screening criteria; instead, the candidates were prioritized qualitatively by integrating MS/MS identification confidence, database-supported sequence identification, predicted non-toxicity, physicochemical and sequence diversity, and docking results. Docking was therefore used as one of the prioritization criteria rather than as the sole basis for peptide selection.

Table 1. LC–MS/MS and in silico characteristics of candidate peptides.

No.	Sequence	Length	*m/z*	Mass (Da)	Vina (kcal/mol)	TIPred Score	ToxinPred Result
1	EEGSPDWRR	9	377.85	1131.28	−9.971	0.393	Non-toxic
2	TPGPTGPIK	9	434.25	867.14	−9.965	0.304	Non-toxic
3	VTPPHVE	7	389.71	777.97	−9.958	0.586	Non-toxic
4	LDKPGPPT	8	412.73	824.05	−9.519	0.253	Non-toxic
5	EKLGDLYR	8	497.27	993.24	−9.505	0.709	Non-toxic
6	LREQFE	6	821.42	820.98	−9.494	0.312	Non-toxic
7	EVPLPPHK	8	458.77	916.20	−9.412	0.374	Non-toxic
8	VIDVPGPVK	9	462.28	923.25	−9.406	0.322	Non-toxic
9	EVPLPPSK	8	433.76	866.13	−9.364	0.216	Non-toxic
10	LDKPGPPA	8	397.73	794.02	−9.361	0.206	Non-toxic

2.7. Experimental Validation of Synthesized Candidate Peptides

Five candidate peptides, including EKLGDLYR, LDKPGPPT, VTPPHVE, TPGPTGPIK, and EEGSPDWRR, were synthesized and evaluated for tyrosinase-inhibitory activity. At a final concentration of 3.33 mM, the five peptides exhibited significantly different inhibition rates, demonstrating a clear sequence-dependent effect (Table 2). VTPPHVE showed the highest tyrosinase inhibition, followed by EKLGDLYR and EEGSPDWRR, whereas LDKPGPPT and TPGPTGPIK were less active. The relatively strong activity of VTPPHVE may be associated with its shorter chain length and the presence of Val, Pro, His, and Glu residues, which provide hydrophobic, polar, and potentially metal-interacting groups [7]. However, residue composition alone cannot fully explain peptide activity because peptide conformation, side-chain accessibility, and binding orientation may also contribute.

Table 2. Experimental validation of synthesized candidate peptides and kojic acid.

Peptide	Tyrosinase Inhibition at 3.33 mM (%)	Tyrosinase-Inhibition IC_{50} (μM)	Apparent Cu^{2+}-Chelation IC_{50} (μM)
EEGSPDWRR	51.99 ± 0.35 ^{b}	314.87 ± 1.16 ^{d}	433.57 ± 1.10 ^{d}
VTPPHVE	59.39 ± 0.28 ^{a}	113.41 ± 0.48 ^{b}	141.54 ± 0.56 ^{b}
LDKPGPPT	24.50 ± 0.82 ^{c}	—	—
TPGPTGPIK	17.68 ± 0.46 ^{d}	—	—
EKLGDLYR	53.58 ± 0.56 ^{b}	274.87 ± 0.86 ^{c}	322.78 ± 1.10 ^{c}
Kojic acid	—	11.26 ± 0.11 ^{a}	32.06 ± 0.14 ^{a}

For the tyrosinase inhibition assay, all peptide and kojic acid concentrations are expressed as final concentrations in the reaction mixture. Values are expressed as mean ± SD (n = 3). Different superscript lowercase letters within the same column indicate significant differences ($p < 0.05$). Kojic acid was used as the positive control for IC_{50} determination. —, not determined.

Based on the initial screening, VTPPHVE, EKLGDLYR, and EEGSPDWRR were selected for MS/MS confirmation and IC_{50} determination. The corresponding concentration–response curves and nonlinear fitting results were provided in Figure S2 and Table S7.

VTPPHVE showed the lowest IC_{50} value for tyrosinase inhibition (113.41 ± 0.48 μM) among the synthesized peptides and exhibited the strongest apparent Cu^{2+}-chelating ability among the synthesized candidates (141.54 ± 0.56 μM) (Table 2). The IC_{50} value of VTPPHVE was lower than those reported for previously identified food-derived tyrosinase-inhibitory peptides (0.21–3.22 mM) [19–22]. However, direct comparisons should be interpreted with caution because the assay conditions differed among studies. The TIPred scores did not fully correspond to the experimental activity ranking: although EKLGDLYR had the highest score (0.709), VTPPHVE showed the strongest activity despite ranking second (0.586), indicating that TIPred provided useful sequence-level prioritization but was insufficient for accurately ranking experimental inhibitory potency.

2.8. Functional Activity Retention of Synthesized Tyrosinase-Inhibitory Peptides

2.8.1. Retention of Tyrosinase-Inhibitory Activity After pH Treatment

The tyrosinase-inhibitory activities of the five synthesized peptides were evaluated after pH treatment (Figure 6A). The peptides showed sequence-dependent responses across pH 2–10. EKLGDLYR and EEGSPDWRR showed greater variation under alkaline conditions, whereas LDKPGPPT and TPGPTGPIK remained comparatively weak inhibitors. VTPPHVE maintained inhibitory activity above 51% across the tested pH range, with no significant differences among pH treatments ($p > 0.05$).

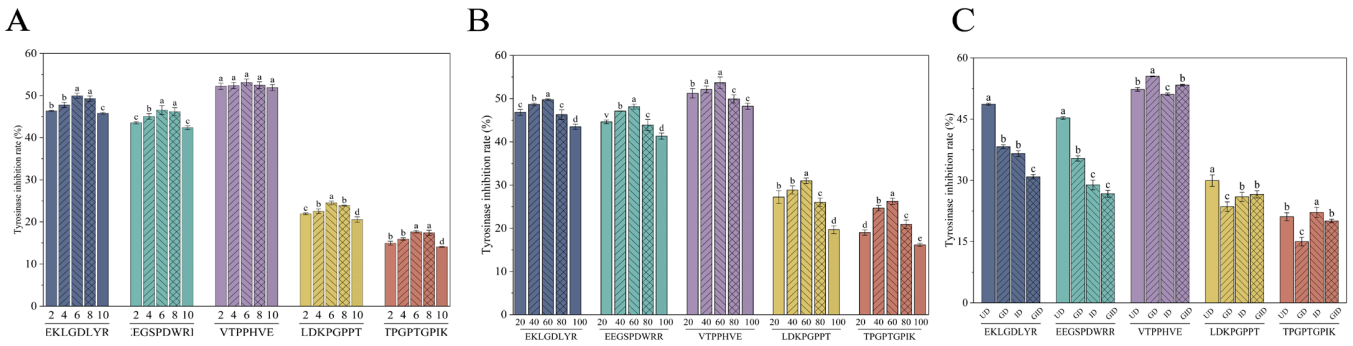


Figure 6. Stability evaluation of synthesized tyrosinase-inhibitory peptides. (**A**) Effect of pH treatment on the tyrosinase inhibitory activity of synthesized peptides. (**B**) Effect of thermal treatment on the tyrosinase inhibitory activity of synthesized peptides. (**C**) Changes in tyrosinase inhibitory activity of synthesized peptides after simulated gastrointestinal digestion. UD, undigested peptide; GD, gastric digestion; ID, intestinal digestion; GID, gastrointestinal digestion. Different lowercase letters indicate significant differences among treatments of the same peptide ($p < 0.05$).

These results indicate strong retention of VTPPHVE bioactivity after short-term pH exposure. Because peptide integrity and conformational state were not directly measured, the data should not be interpreted as proof that the molecular structure of VTPPHVE remained unchanged. The observation is nevertheless relevant to marine peptide applications because pH-dependent activity retention is an important consideration during formulation and processing [23].

2.8.2. Retention of Tyrosinase-Inhibitory Activity After Thermal Treatment

Thermal treatment produced sequence-dependent changes in tyrosinase inhibition (Figure 6B). EKLGDLYR and EEGSPDWRR showed increased activity up to 60 °C followed by a decline at higher temperatures, while LDKPGPPT and TPGPTGPIK showed larger activity losses after high-temperature exposure. VTPPHVE retained comparatively high inhibitory activity throughout 20–100 °C, reaching its highest level at 60 °C and remaining above 48% after treatment at 100 °C. Significant differences were observed among temper-

ature treatments ($p < 0.05$); however, no significant differences were observed between 40 and 60 °C or between 80 and 100 °C ($p > 0.05$). The results support thermal retention of VTPPHVE-mediated bioactivity under the conditions tested. As with the pH experiment, this assay measured functional activity rather than chemical integrity of the intact peptide. Similar processing-oriented evaluation of marine bioactive peptides has been used to assess their suitability for functional-product development [24].

2.8.3. Retention of Tyrosinase-Inhibitory Activity After Simulated Gastrointestinal Digestion

Tyrosinase-inhibitory activity was measured after simulated gastric digestion (GD), intestinal digestion (ID), and sequential gastrointestinal digestion (GID) (Figure 6C). EKLGDLYR, EEGSPDWRR, TPGPTGPIK, and LDKPGPPT showed varying losses of activity after digestion, indicating that the biological response of each peptide sequence was differently affected by the digestive treatments.

VTPPHVE-containing digestion mixtures retained apparent tyrosinase-inhibitory activity above 50% after gastric digestion (GD), intestinal digestion (ID), and sequential gastrointestinal digestion (GID), with the GID-treated mixture showing activity comparable to that of the undigested control. These results indicate that tyrosinase-inhibitory activity remained detectable following simulated gastrointestinal digestion [25]. However, the observed inhibitory activity of the digestion mixture cannot be solely attributed to intact VTPPHVE, since both residual native peptide and newly formed active fragments after digestion may contribute to the bioactivity. Therefore, the results support the retention of apparent inhibitory activity after simulated digestion.

2.9. Mechanistic Characterization of VTPPHVE

2.9.1. Enzyme Inhibition Kinetics

The initial rate increased hyperbolically with L-DOPA concentration at each VTPPHVE level, but the fitted Michaelis–Menten curves progressively shifted as inhibitor concentration increased (Figure 7A). The apparent Vmax decreased from 0.057 ΔA475/min in the absence of VTPPHVE to 0.042 ΔA475/min at 120 μM, whereas the apparent Km increased overall from 0.88296 to 1.75794 mM. Intermediate VTPPHVE concentrations produced the same general pattern, with Vmax values of 0.055, 0.052, and 0.043 ΔA_{475}/min and Km values of 1.143, 1.260, and 1.255 mM at 15, 30, and 60 μM, respectively. The apparent Michaelis–Menten parameters obtained at each VTPPHVE concentration are summarized in Table S6.

The simultaneous reduction in apparent Vmax and increase in apparent Km is inconsistent with a purely competitive or purely non-competitive model and is consistent with mixed-type inhibition. The Lineweaver–Burk plots likewise showed inhibitor-dependent changes in both slope and intercept, with the fitted lines not converging on either coordinate axis (Figure 7B). Similar mixed-type behavior has been reported for other food-derived tyrosinase-inhibitory peptides [9,10]. These kinetic results provide experimental evidence that VTPPHVE alters both substrate affinity and catalytic capacity, while not by themselves identifying a unique physical binding site. Global nonlinear fitting further supported the mixed-type inhibition model. Among the four models tested, the mixed-type model showed the highest R^2 (0.9829) and the lowest AICc (−636.43), with Ki and Ki′ values of 70.16 and 289.28 μM, respectively (Table S9). These results provide additional support for the mixed-type inhibition proposed from the kinetic plots.

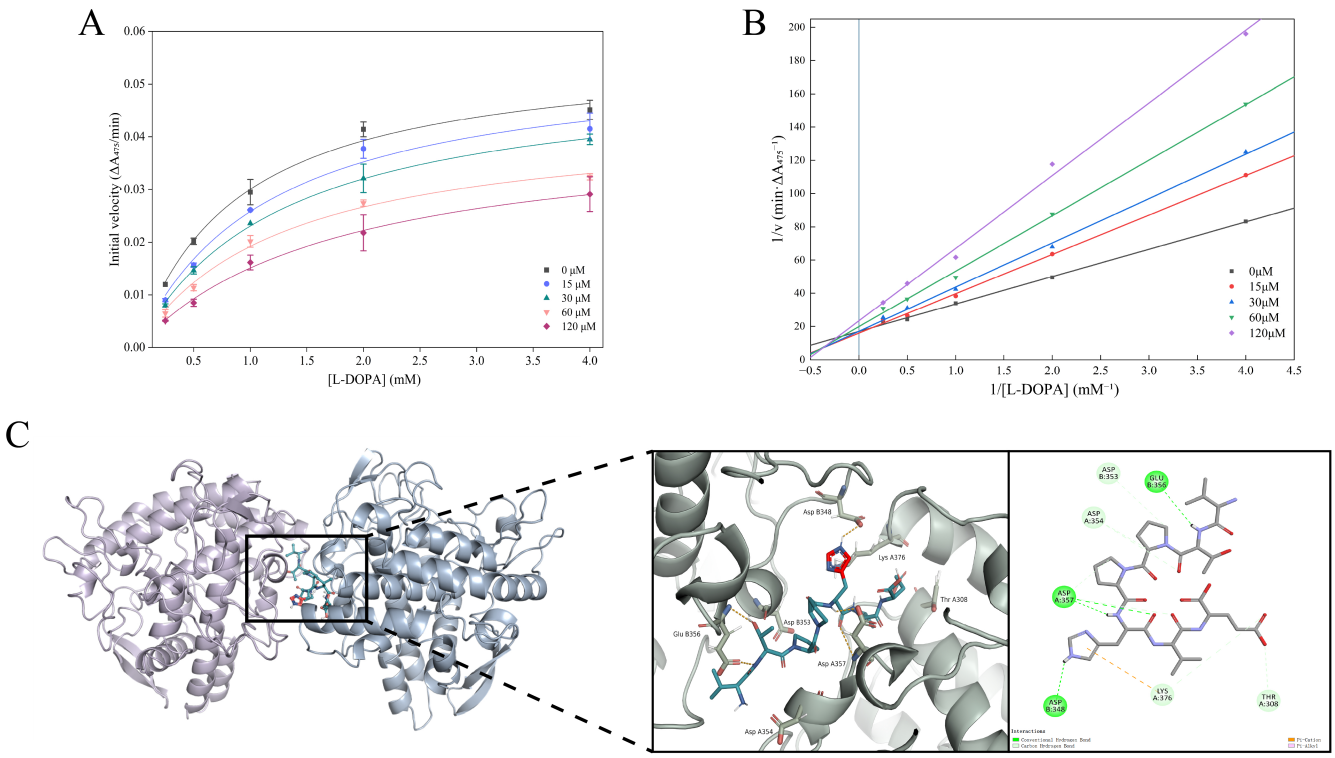


Figure 7. Enzyme inhibition kinetics and molecular docking analysis of VTPPHVE against mushroom tyrosinase. (**A**) Michaelis–Menten plots obtained at VTPPHVE concentrations of 0, 15, 30, 60, and 120 μM using L-DOPA concentrations of 0.25–4.0 mM. (**B**) Corresponding Lineweaver–Burk plots used as a complementary graphical assessment of the inhibition pattern. (**C**) Overall docking pose, enlarged three-dimensional interaction view, and corresponding two-dimensional interaction map of VTPPHVE in an inter-chain surface region spanning H-subunit chains A and B of the deposited 2Y9X structure.

2.9.2. Molecular Docking Analysis of VTPPHVE

Detailed docking of VTPPHVE to the deposited multichain mushroom tyrosinase structure (PDB ID: 2Y9X) placed the peptide in an inter-chain surface region spanning polyphenol oxidase chains A and B, both of which correspond to H subunits (Figure 7C). The overall docking pose, enlarged three-dimensional interaction view, and corresponding two-dimensional interaction map illustrate the predicted binding mode and surrounding residues. The selected pose formed polar contacts with Thr A308, Asp A354, Asp A357, Lys A376, Asp B348, Asp B353, and Glu B356. This region is spatially separated from the canonical binuclear copper-binding site and lies within a C-terminal surface region of the H subunits.

The original structural characterization of A. bisporus tyrosinase described an H_2L_2 organization and an H–H interface involving residues Asp312, Asp336, Gln351, and Asp353 [26]. The predicted VTPPHVE-binding region lies close to the reported H–H interface and includes Asp353 among the residues surrounding the selected peptide pose. Nevertheless, the docking result alone is insufficient to confirm that VTPPHVE occupies the structurally defined H–H interface or perturbs the oligomeric organization of tyrosinase. Therefore, the predicted pose was interpreted as a plausible non-catalytic inter-chain surface-binding mode rather than a verified allosteric site.

None of the canonical copper-coordinating residues His61, His85, His94, His259, His263, or His296 directly participated in the selected pose. Thus, the docking result does not support direct occupation of the canonical binuclear copper-binding site. The predicted non-catalytic binding mode is compatible with the experimentally observed

mixed-type inhibition but does not by itself establish an allosteric mechanism. The exclusion of catalytic Cu ions may omit potential metal-coordination and electrostatic effects, while the A/B-chain model may not fully represent the quaternary environment of the complete tyrosinase complex. Therefore, the docking and MD results should be interpreted as reflecting VTPPHVE binding and stability within the selected structural model rather than the complete holoenzyme.

2.9.3. Molecular Dynamics Simulation

The dynamic behavior of the predicted VTPPHVE–tyrosinase complex was further evaluated by a 100 ns MD simulation (Figure 8). MD simulations have been increasingly used to complement static docking by evaluating the conformational stability and dynamic behavior of food-derived peptide–enzyme complexes [27–29]. The RMSD of the VTPPHVE–tyrosinase complex exhibited an initial conformational adjustment during the early stage of the trajectory, followed by comparatively restricted fluctuations during the later simulation period (Figure 8A). This behavior suggests that the docked complex underwent structural relaxation before reaching a relatively persistent conformational regime rather than remaining unchanged from its initial docking geometry.

Residue-level RMSF analysis revealed that most protein regions displayed limited fluctuations, whereas several terminal and loop regions showed greater local mobility (Figure 8B). The two protein chains also exhibited different fluctuation profiles, indicating heterogeneous conformational flexibility within the complex. Because an apo-tyrosinase trajectory was not simulated, these RMSF differences were interpreted as intrinsic mobility within the peptide-bound system rather than evidence that VTPPHVE reduced global protein flexibility [30].

The Rg and SASA profiles showed noticeable changes during the initial relaxation period but subsequently fluctuated within comparatively restricted ranges (Figure 8C,D), indicating the absence of continuous expansion or collapse of the protein structure during the later trajectory. Intermolecular hydrogen bonds between VTPPHVE and tyrosinase were dynamically formed and disrupted throughout the simulation (Figure 8E). Although the number of hydrogen bonds varied with time, recurrent peptide–protein contacts remained detectable during the later simulation stage, supporting persistent interaction of the flexible peptide with the predicted interfacial region.

The RMSD–Rg free-energy landscape further revealed a dominant low-energy conformational region together with neighboring metastable states (Figure 8F,G), suggesting repeated sampling of a restricted conformational ensemble after the initial structural adjustment [28]. Taken together, the trajectory analyses indicate that the docking-derived VTPPHVE–A/B H-subunit complex remained dynamically stable throughout the 100 ns simulation. The overall trajectory behavior supports the persistence of the predicted intersubunit binding pose and provides complementary dynamic evidence for the docking results. These findings suggest that the A/B-subunit interface represents a plausible binding region for VTPPHVE within the modeled structure. The MD simulation further characterizes the peptide–protein interactions in the copper-free model, providing insight into the dynamic behavior of the predicted complex.

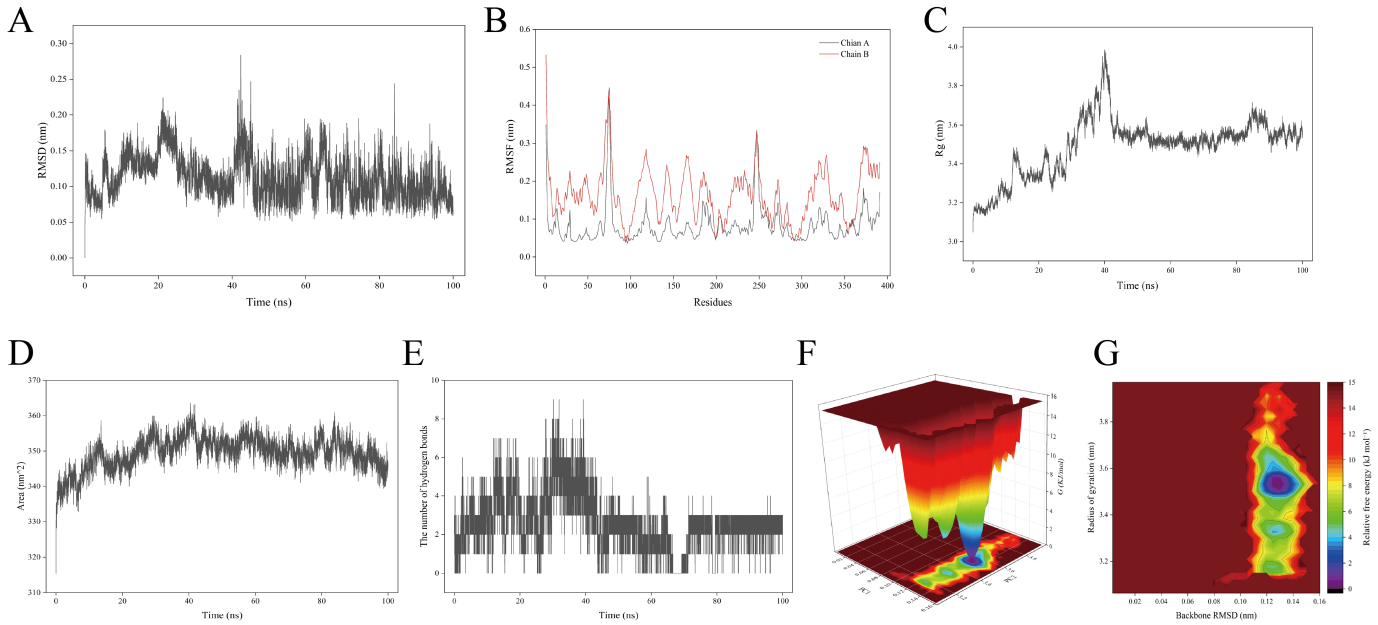


Figure 8. Molecular dynamics analysis of the docking-derived VTPPHVE–tyrosinase A/B-chain model during a 100 ns simulation. (**A**) Root-mean-square deviation (RMSD) of the VTPPHVE–tyrosinase complex. (**B**) Residue-level root-mean-square fluctuation (RMSF) profiles of tyrosinase chains A and B. (**C**) Radius of gyration (Rg). (**D**) Solvent-accessible surface area (SASA). (**E**) Number of intermolecular hydrogen bonds between VTPPHVE and tyrosinase. (**F**) Three-dimensional Gibbs free-energy landscape and (**G**) corresponding two-dimensional free-energy contour map constructed from complex RMSD and Rg. In (**F**,**G**), the color gradient represents Gibbs free energy, with green, yellow, and red indicating increasing energy levels. The simulation was used to evaluate the dynamic behavior of the docking-derived A/B H-subunit model rather than to reproduce the complete native oligomeric assembly. Because the catalytic Cu ions were not parameterized in the MD system, the trajectory analysis does not provide evidence for direct copper coordination or establish the physiological binding site of VTPPHVE.

3. Materials and Methods

3.1. Materials and Reagents

Fresh golden pompano were purchased from a Hema Fresh (Freshippo) supermarket in Guangzhou, Guangdong, China (Figure S3). The external morphology was examined by a specialist in fish taxonomy at the College of Animal Science, Zhongkai University of Agriculture and Engineering, and was consistent with *T. anak* [12]. Alkaline protease, bromelain, papain, neutral protease, Flavourzyme, trypsin, o-phthalaldehyde (OPA), mushroom tyrosinase, 2,2′-azino-bis(3-ethylbenzothiazoline-6-sulfonic acid) diammonium salt (ABTS), bovine serum albumin (BSA), L-serine, L-3,4-dihydroxyphenylalanine (L-DOPA), kojic acid, potassium persulfate, copper(II) sulfate pentahydrate ($CuSO_4 \cdot 5H_2O$), and pyrocatechol violet were purchased from Shanghai Macklin Biochemical Technology Co., Ltd. (Shanghai, China). Artificial gastric fluid and artificial intestinal fluid used for simulated gastrointestinal digestion were purchased from Shanghai Yuanye Biotechnology Co., Ltd. (Shanghai, China).

3.2. Preparation of Golden Pompano Muscle Substrate

The fresh fish were transported to the laboratory on ice and immediately decapitated, eviscerated, and deboned. The dorsal muscle was collected, minced into a homogeneous paste using a meat grinder, divided into appropriate portions, and stored at −20 °C until further use.

3.3. Screening of Proteases and Optimization of the Neutral Protease–Papain Ratio

3.3.1. Screening of Commercial Proteases Based on Hydrolysis Performance

The frozen minced muscle was thawed at 4 °C and homogenized with deionized water at a solid-to-liquid ratio of 1:5 (*w*/*v*). Neutral protease, alkaline protease, Flavourzyme, papain, bromelain, and trypsin were evaluated individually under the temperature, initial pH, and hydrolysis-time conditions listed in Table S1. Before enzyme addition, the pH of each suspension was adjusted with 1.0 M NaOH or 1.0 M HCl; pH was not further controlled during hydrolysis. Each enzyme was added at 1000 U/g substrate, where the substrate mass referred to the wet weight of minced golden pompano muscle. The mass of each enzyme preparation was calculated from its activity stated by the supplier. Hydrolysis was terminated at 95 °C for 10 min. After cooling, the samples were centrifuged at 9727× *g* for 10 min at 4 °C, and the supernatants were collected for determination of degree of hydrolysis (DH) and soluble peptide concentration (SPC).

3.3.2. Optimization of the Neutral Protease-to-Papain Ratio

Neutral protease and papain were combined at mass ratios of 3:1, 2:1, 1:1, 1:2, and 1:3. For each treatment, the masses of the two commercial enzyme preparations were calculated from their supplier-declared specific activities so that the sum of the nominal enzyme activities was maintained at 1000 U/g substrate. The exact amount and nominal activity contribution of each enzyme are provided in Table S1. The substrate suspension was adjusted to pH 7.0 before simultaneous enzyme addition and hydrolyzed at 50 °C for 5 h. Hydrolysis was terminated at 95 °C for 10 min, followed by cooling and centrifugation at 9727× *g* for 10 min at 4 °C. The neutral protease-to-papain ratio used in subsequent experiments was selected according to the combined DH and SPC.

3.4. Determination of Hydrolysis-Performance Indices

3.4.1. Soluble Peptide Concentration

The SPC of the hydrolysates was determined using the Biuret colorimetric assay with slight modifications [31]. Briefly, the hydrolysate samples were appropriately diluted with deionized water to ensure that the absorbance values fell within the linear range of the standard curve. An aliquot of 1.0 mL of the diluted sample was mixed with 4.0 mL of Biuret reagent, vortexed thoroughly, and incubated at 37 °C for 20 min. After incubation, the absorbance was measured at 540 nm using a UV–Vis spectrophotometer, with deionized water used as the blank. BSA solutions ranging from 0 to 10.0 mg/mL were used to construct the standard curve. The SPC was calculated from the standard curve and expressed as mg BSA equivalents/mL.

3.4.2. Degree of Hydrolysis

The DH was determined using the o-phthaldialdehyde (OPA) method, which quantifies primary amino groups released during hydrolysis [32]. Lyophilized hydrolysate was dissolved in deionized water and diluted to the linear range. Sample solution (0.4 mL) was mixed with 3.0 mL of freshly prepared OPA reagent, vortexed for 5 s, and reacted for 2 min at room temperature in the dark. Absorbance was measured at 340 nm against a reagent blank.

L-Serine was used to construct the calibration curve for OPA-reactive amino groups. Serine amino equivalents were calculated from the standard curve, and DH was calculated using Equation (1).

$$\mathrm{DH}(\%) = \frac{\mathrm{h}}{\mathrm{h_{tot}}} \times 100;\ \mathrm{h} = \frac{\mathrm{SerineNH_2} - \beta}{\alpha} \quad (1)$$

where h is the number of hydrolyzed peptide bonds per gram of protein (mmol g^{-1}), htot is the total number of peptide bonds per gram of substrate protein (8.4 mmol g^{-1}), SerineNH_2 is the concentration of OPA-reactive amino groups expressed as serine amino equivalents (mmol g^{-1} protein), and α and β are the system constants (1.00 and 0.40, respectively).

3.5. Ultrasound-Assisted Dual-Enzyme Hydrolysis

3.5.1. Single-Factor Experiments

Single-factor experiments were conducted to determine the appropriate ranges of the key variables for ultrasound-assisted enzymatic hydrolysis. The minced golden pompano muscle was mixed with deionized water at the designated solid-to-liquid ratio, after which the suspension was adjusted to pH 7.0. The suspension was then subjected to ultrasound pretreatment using an XO-SM100 ultrasonic-microwave synergistic reaction workstation (Nanjing Xianou Instrument Manufacturing Co., Ltd., Nanjing, China) at the designated power and treatment time, followed immediately by the simultaneous addition of neutral protease and papain at a mass ratio of 2:1. Enzymatic hydrolysis was performed at 50 °C for the designated time, and the reaction was terminated by heating at 95 °C for 10 min. The reference conditions were a solid-to-liquid ratio of 1:5 (*w*/*v*), a combined enzyme dosage of 1000 U/g substrate, an enzymatic hydrolysis time of 5 h, an ultrasonic power of 200 W, and an ultrasonic time of 20 min. The investigated levels were 1:4–1:8 (*w*/*v*) for the solid-to-liquid ratio, 600–1400 U/g substrate for enzyme dosage, 3–7 h for enzymatic hydrolysis time, 100–500 W for ultrasonic power, and 10–30 min for ultrasonic time.

3.5.2. Response Surface Optimization and Experimental Verification

Before activity determination, all hydrolysates were standardized to the same dry-mass concentration (10 mg/mL). Based on the single-factor results, the solid-to-liquid ratio and ultrasonic power were fixed at 1:4 (*w*/*v*) and 200 W, respectively. A three-factor, three-level Box–Behnken design was generated using Design-Expert 13.0 to evaluate the effects of enzyme dosage (A, 800–1200 U/g substrate), enzymatic hydrolysis time (B, 4–6 h), and ultrasonic time (C, 15–25 min; Table S2) on tyrosinase inhibition. The design comprised 17 runs, including five center-point replicates. The experimental results were fitted to a second-order polynomial model, and model adequacy was evaluated by analysis of variance, coefficient of determination, adjusted coefficient of determination, and lack-of-fit testing. The predicted optimal conditions were experimentally verified in triplicate.

3.6. Validation of the Optimized UAE Process Against Individual Treatments

To evaluate whether the optimized UAE process provided an advantage over the individual treatments, four groups were prepared: untreated control, ultrasound treatment alone (US), enzymatic hydrolysis alone (EN), and ultrasound-assisted enzymatic hydrolysis (UAE). Except for the designated treatment variables, the solid-to-liquid ratio, substrate mass, processing duration, centrifugation, lyophilization, and assay concentration were maintained consistently among groups. After identical centrifugation, the lyophilized samples were redissolved at 10 mg/mL, corresponding to a final assay concentration of 3.33 mg/mL.

3.7. In Vitro Bioactivity Assays

3.7.1. Tyrosinase-Inhibitory Activity

Tyrosinase-inhibitory activity was measured using mushroom tyrosinase and L-DOPA with modifications from Deng [33]. Sample solution (100 µL) and mushroom tyrosinase solution (100 µL, 125 U/mL in 0.05 M phosphate buffer, pH 6.8) were combined in a 96-well plate and pre-incubated at 25 °C for 5 min. L-DOPA solution (100 µL, 5.07 mM in the same

buffer) was then added. After 5 min at 25 °C, dopachrome formation was measured at 475 nm using a microplate reader. Because L-DOPA was used as the substrate, the present assay primarily reflects the diphenolase activity of tyrosinase; monophenolase activity was not evaluated in this study. Kojic acid served as the positive control. Control and sample blanks without tyrosinase were included to correct for intrinsic sample absorbance. Tyrosinase inhibition was calculated using Equation (2):

$$\text{Tyrosinase-inhibitory activity (\%)} = \left[1 - \frac{C - D}{A - B}\right] \times 100 \quad (2)$$

where A represents the absorbance of the control (without the test sample); B represents the absorbance of the control blank (without both the test sample and tyrosinase); C represents the absorbance of the sample (with the test sample, tyrosinase, and L-DOPA); and D represents the absorbance of the sample blank (without tyrosinase, used to correct for the background absorbance of the sample itself). IC_{50} values were determined by nonlinear regression using a four-parameter logistic model with a variable slope in GraphPad Prism version 11.1.0 (GraphPad Software, Boston, MA, USA).

3.7.2. ABTS Radical-Scavenging Activity

ABTS radical-scavenging activity was determined with modifications based on the previous report [34]. ABTS solution (7.0 mM) and potassium persulfate solution (2.45 mM) were mixed at 1:1 (v/v) and incubated in the dark at room temperature for 12–16 h. The resulting ABTS$\bullet^+$ solution was diluted with absolute ethanol to an absorbance of 0.70 ± 0.02 at 734 nm. Sample solution (20 µL) was mixed with 180 µL of ABTS working solution in a 96-well plate, incubated in the dark for 10 min at room temperature, and measured at 734 nm. A sample-background well, in which ABTS working solution was replaced with ethanol, was included. Scavenging activity was calculated using Equation (3):

$$\text{ABTS radical-scavenging activity (\%)} = \left[1 - \frac{A_1 - A_2}{A_0}\right] \times 100 \quad (3)$$

where A_1 is the absorbance of the sample plus ABTS working solution, A_2 is the absorbance of the sample-background well, and A_0 is the absorbance of the solvent control plus ABTS working solution.

3.7.3. Apparent Cu^{2+}-Chelating Activity

Apparent Cu^{2+}-chelating activity was determined using the pyrocatechol violet method with slight modifications [35]. Peptide sample (10 µL), 1 mM $CuSO_4 \cdot 5H_2O$ (10 µL), 50 mM sodium acetate buffer (pH 6.0; 270 µL), and 4 mM pyrocatechol violet (6 µL) were mixed. Absorbance was measured at 632 nm. Deionized water was substituted for the sample in the control. Chelating activity was calculated using Equation (4):

$$\text{Apparent } Cu^{2+}\text{-chelating activity (\%)} = \left[\frac{A - B}{A}\right] \times 100 \quad (4)$$

where A represents the absorbance of the control group (where deionized water replaced the sample) at 632 nm, and B represents the absorbance of the sample group at 632 nm.

3.8. Activity-Guided Ultrafiltration of the Optimized Hydrolysate

The optimized hydrolysate was sequentially fractionated using ultrafiltration membranes with molecular weight cutoffs of 10, 5, and 3 kDa to obtain >10 kDa, 5–10 kDa, 3–5 kDa, and <3 kDa fractions. Each fraction was collected, lyophilized, and stored at −20 °C. Before activity assays, all fractions were dissolved at the same dry-mass concentration to permit direct comparison.

3.9. Acid-Hydrolyzable Amino Acid Composition of Molecular Weight Fractions

The acid-hydrolyzable amino acid composition was determined as previously reported with slight modifications [36]. Sample solution (1 mL) was mixed with 9 mL of 6 M HCl in a hydrolysis tube. After nitrogen purging and vacuum sealing, hydrolysis was conducted at 110 °C for 22 h. The hydrolysate was cooled, filtered, diluted to 50 mL, and a 2 mL aliquot was evaporated to dryness. The residue was re-dissolved in deionized water, evaporated again, and finally brought to 1.6 mL. After filtration through a 0.22 µm membrane, amino acids were analyzed using an LA8080 amino acid analyzer (Hitachi, Tokyo, Japan). Because conventional acid hydrolysis does not quantitatively recover tryptophan and may affect cysteine and methionine, the resulting profile was interpreted as acid-hydrolyzable amino acid composition rather than complete amino acid composition.

3.10. LC–MS/MS Identification and Candidate-Peptide Prioritization

3.10.1. LC-MS/MS Analysis

The lyophilized <3 kDa peptide fraction was reconstituted in 0.1% (*v*/*v*) formic acid, centrifuged at 12,000× *g* for 15 min at 4 °C, desalted using a C18 StageTip, dried under vacuum, and reconstituted in 0.1% formic acid before nanoLC–MS/MS analysis.

Peptides were separated using an EASY-nLC 1200 system coupled to a Q Exactive Plus Orbitrap mass spectrometer, both manufactured by Thermo Fisher Scientific (Bremen, Germany). The mass spectrometer was equipped with a nano-electrospray ionization source. Mobile phase A was 0.1% formic acid in water, and mobile phase B was 80% acetonitrile containing 0.1% formic acid. A 3 µL aliquot was loaded onto an Acclaim PepMap 100 C18 trapping column (3 µm, 75 µm i.d. × 2 cm) and separated on an Acclaim PepMap C18 analytical column (2 µm, 75 µm i.d. × 25 cm) at 40 °C and 300 nL/min. The 60 min gradient was 2–35% B over 47 min, 35–100% B over 1 min, and 100% B for 12 min. A blank solvent run was performed between samples to minimize carryover.

The mass spectrometer was calibrated before analysis and operated in positive-ion data-dependent acquisition mode. Full MS scans were acquired over m/z 300–1500 at a resolution of 70,000 at m/z 200, with an automatic gain control target of 3×10^6 and a maximum injection time of 100 ms. The 20 most intense precursor ions were selected for higher-energy collisional dissociation at a normalized collision energy of 28 and an isolation window of 1.6 m/z. MS/MS spectra were acquired at a resolution of 17,500, with an automatic gain control target of 1×10^5, a maximum injection time of 50 ms, and a dynamic exclusion time of 30 s.

Raw data were processed using PEAKS Studio 13.0 (Bioinformatics Solutions Inc., Waterloo, ON, Canada) and searched against the NCBI RefSeq protein sequence database associated with the *Trachinotus anak* genome assembly CSIRO_AGI_Tana_v1 (RefSeq accession GCF_046630095.1), supplemented with common contaminant sequences. Enzyme specificity was set to none. Precursor and fragment ion tolerances were set to 10 ppm and 0.03 Da, respectively. Variable modifications included protein N-terminal acetylation, deamidation of asparagine and glutamine, and oxidation of methionine. A target–decoy strategy was applied, and peptide-spectrum matches and peptide identifications were filtered at a false discovery rate of ≤1%. Confident peptide sequences were exported for subsequent physicochemical-property prediction and stepwise in silico screening.

3.10.2. In Silico Screening and Physicochemical Characterization of Candidate Peptides

LC–MS/MS-identified sequences were prioritized using a predefined stepwise workflow. Peptides containing no more than ten residues and a PEAKS −10lgP score > 20 were retained. The selected sequences were searched against BIOPEP-UWM (https://biochemia.uwm.edu.pl/biopep/start_biopep.php; accessed on 20 May 2025) to

determine whether they were listed as previously reported bioactive peptides; absence from BIOPEP-UWM was interpreted only as absence from that database, not as proof of global novelty. TIPred (https://pmlabstack.pythonanywhere.com/TIPred; accessed on 20 May 2025) was used as a target-specific auxiliary model to evaluate the likelihood of tyrosinase-inhibitory activity. Because its output represents a sequence-based classification probability rather than a quantitative estimate of inhibitory potency, the prediction score was used as a supportive descriptor rather than a fixed exclusion criterion. Molecular weight, theoretical isoelectric point, net charge, and hydrophobicity were calculated using PepDraw (https://pepdraw.com/; accessed on 20 May 2025), and potential toxicity was assessed using ToxinPred (https://webs.iiitd.edu.in/raghava/toxinpred/; accessed on 20 May 2025).

All shortlisted candidates were subjected to preliminary docking, which was used as an important structural prioritization criterion. Candidate selection followed a stepwise rather than quantitatively weighted scoring strategy, integrating MS/MS confidence, peptide length, database information, target-specific prediction scores, physicochemical properties, predicted toxicity, docking performance, and sequence diversity. No formal numerical weights were assigned because these parameters represent different types of evidence and are not directly comparable. The five peptides selected for synthesis represented candidates with favorable overall in silico profiles, with docking performance serving as an important criterion for experimental prioritization.

3.11. Peptide Synthesis and Experimental Validation

Five candidate peptides were synthesized by solid-phase peptide synthesis (Sangon Biotech Co., Ltd., Shanghai, China). Purity was reported by the supplier as >98% based on HPLC and MS. The synthesized peptides were dissolved in deionized water or assay buffer immediately before analysis and used for tyrosinase-inhibition and Cu^{2+}-chelation assays.

3.12. Retention of Tyrosinase-Inhibitory Activity of Synthesized Tyrosinase-Inhibitory Peptides

3.12.1. pH Treatment

The pH stability of selected peptides was evaluated according to a previously reported method with slight modifications. Peptide solutions were adjusted to different pH values (2.0, 4.0, 6.0, 8.0, and 10.0) using appropriate concentrations of HCl or NaOH and maintained at room temperature for 2 h. Subsequently, the samples were readjusted to the original assay pH using phosphate buffer. The tyrosinase-inhibitory activity of each treated sample was then measured as described in Section 3.7.1. Untreated peptide solutions were assayed in parallel as controls, and the inhibition rates were calculated using the same method.

3.12.2. Thermal Stability

Thermal stability was evaluated by incubating peptide solutions at different temperatures (20, 40, 60, 80, and 100 °C) for 30 min. After cooling to room temperature, the treated samples were immediately subjected to tyrosinase-inhibitory activity determination as described in Section 3.7.1. Untreated peptide solutions were assayed in parallel as controls, and the inhibition rates were calculated using the same method.

3.12.3. Simulated Gastrointestinal Digestion Stability of Selected Peptides

The simulated gastrointestinal digestion stability of selected peptides was evaluated according to a previously reported method with slight modifications [37]. The SGF and SIF were used to simulate gastric and intestinal digestion conditions, respectively. The SGF was based on the USP formulation and contained pepsin (3.2 g/L) under acidic conditions (pH 1.2). The SIF contained trypsin (0.464 g/L) and phosphate salts under weak alkaline conditions (pH 6.8).

Briefly, peptide solutions were mixed with SGF at a volume ratio of 1:1 (*v*/*v*) and incubated at 37 °C for 2 h. After gastric digestion, the pH of the digests was adjusted to 6.8, followed by incubation with SIF at a volume ratio of 1:1 (*v*/*v*) for another 2 h. Sequential gastrointestinal digestion (GID) was performed by consecutive gastric and intestinal digestion under the same conditions. After completion of digestion, enzymatic reactions were terminated by heating the samples in a boiling water bath for 10 min. The samples were immediately cooled and directly subjected to tyrosinase-inhibitory activity determination using the same procedure described in Section 3.7.1, with L-DOPA as the substrate and absorbance measured at 475 nm. The digested samples were not normalized to an equivalent peptide concentration before the assay, and digestion-fluid blanks were not included.

3.13. Enzyme Inhibition Kinetics of VTPPHVE

The inhibition kinetics of VTPPHVE was evaluated using L-DOPA as the substrate under the same buffer and temperature conditions used for the tyrosinase assay. Final VTPPHVE concentrations of 0, 15, 30, 60, and 120 μM were tested against L-DOPA concentrations of 0.25, 0.50, 1.00, 2.00, and 4.00 mM. VTPPHVE solution (100 μL) was pre-incubated with mushroom tyrosinase working solution (100 μL, 125 U/mL) at 25 °C for 5 min, after which L-DOPA (100 μL) was added to initiate the reaction. Absorbance at 475 nm was recorded every 30 s for 10 min. Initial reaction rates (v, ΔA_{475}/min) were calculated by linear regression over the early linear phase (0.5–2.5 min).

Michaelis–Menten curves were fitted by nonlinear regression according to v = Vmax[S]/(Km + [S]) using Origin 2026 (OriginLab Corporation, Northampton, MA, USA), yielding apparent Vmax and Km values at each inhibitor concentration. Lineweaver–Burk plots (1/v versus 1/[S]) were used as a complementary graphical assessment of inhibition pattern. The inhibition type was assigned from the combined changes in apparent Vmax and Km and the intersection behavior of the double-reciprocal lines. To further substantiate the inhibition mode, the initial-rate data obtained at all substrate and inhibitor concentrations were globally fitted to competitive, uncompetitive, noncompetitive, and mixed-type inhibition models by nonlinear regression. The models were compared based on R^2 and AICc, and the corresponding Ki and Ki' values were obtained.

3.14. Molecular Docking of Candidate Peptides with Mushroom Tyrosinase

Molecular docking was performed to investigate the potential interactions between the candidate peptides and mushroom tyrosinase. The crystal structure of *Agaricus bisporus* tyrosinase (PDB ID: 2Y9X) was retrieved from the RCSB Protein Data Bank. The receptor was prepared by removing crystallographic water molecules, the co-crystallized ligand, catalytic Cu ions, and other non-essential heteroatoms, followed by the addition of hydrogen atoms and charges. The peptide structures were prepared as flexible ligands and converted to PDBQT format. Molecular docking was performed using AutoDock Vina 1.2.7 [38,39] with a search box centered at X = −5.129, Y = −0.843, and Z = −67.727 Å, with dimensions of 100 × 100 × 100 Å. The exhaustiveness was set to 16, and 20 binding poses were generated for each peptide. Predicted binding affinities were expressed in kcal/mol, with more negative values indicating more favorable predicted interactions. Representative poses were selected according to the Vina scores and structural plausibility. Protein–peptide interactions were analyzed and visualized using Discovery Studio Visualizer 2019 and PyMOL version 3.1.9 was used for molecular visualization.

3.15. Molecular Dynamics Analysis of the VTPPHVE–Tyrosinase Complex

A 100 ns molecular dynamics (MD) simulation was performed for the selected VTPPHVE–tyrosinase complex using GROMACS 2025. The representative docking pose of VTPPHVE with tyrosinase was used as the starting structure. The protein topology was generated using the AMBER99SB-ILDN force field with the TIP3P water model. The peptide structure was converted to the required GROMACS format and parameterized using ACPYPE with GAFF-compatible parameters. The resulting peptide topology was incorporated into the protein topology to construct the VTPPHVE–tyrosinase complex. The catalytic Cu ions were not included in the MD system because no dedicated metal-site parameterization was performed.

The complex was centered in a cubic simulation box with a minimum distance of 1.0 nm between the solute and the box boundary. The system was solvated with explicit water molecules and electrically neutralized by the addition of Na^+ and Cl^- ions. After energy minimization, the system was subjected sequentially to 100 ps NVT and 100 ps NPT equilibration with positional restraints applied to the solute. The equilibrated complex was subsequently subjected to a 100 ns production MD simulation under periodic boundary conditions. The initial production trajectory was extended to 100 ns from the equilibrated system without reinitializing the coordinates or velocities.

Prior to trajectory analysis, periodic-boundary artifacts were corrected by molecular centering, removal of discontinuous jumps, and rotational/translational fitting. Structural stability and conformational behavior were evaluated using the root-mean-square deviation (RMSD) of the VTPPHVE–tyrosinase complex, residue-level root-mean-square fluctuation (RMSF), radius of gyration (Rg), solvent-accessible surface area (SASA), and intermolecular hydrogen-bond analysis. A Gibbs free-energy landscape (FEL) was further constructed from complex RMSD and Rg coordinates using the GROMACS sham module. The MD calculations were interpreted as an assessment of the dynamic persistence of the predicted peptide–protein complex rather than as evidence of catalytic Cu^{2+} coordination.

3.16. Statistical Analysis

All experiments were independently performed in triplicate, and data are presented as mean ± SD. Statistical analyses were performed using IBM SPSS Statistics 26.0. Differences among groups were analyzed by one-way ANOVA followed by Bonferroni's post hoc test. Differences were considered statistically significant at $p < 0.05$.

4. Conclusions

In this study, an activity-guided workflow identified VTPPHVE as the lead tyrosinase-inhibitory peptide from golden pompano (*T. anak*) muscle proteins. VTPPHVE showed an IC_{50} of 113.41 μM for tyrosinase inhibition and an apparent Cu^{2+}-chelation IC_{50} of 141.54 μM. Its inhibitory bioactivity was retained after pH 2–10 treatment, heating at 20–100 °C, and detectable apparent activity persisted after simulated gastrointestinal treatments, although samples were not normalized for peptide concentration and digestion-fluid blanks were omitted. Enzyme kinetics were consistent with mixed-type inhibition. Exploratory docking placed VTPPHVE at a non-catalytic H-subunit surface/interface region, and a 100 ns MD trajectory supported persistence of peptide–protein contacts after initial structural relaxation. Overall, the study extends VTPPHVE from sequence-level discovery to experimental activity, functional activity retention, and enzyme-level kinetic characterization. Direct binding studies, peptide-fate analysis during digestion, and cellular or food-system validation will be required before nutraceutical, cosmeceutical, or anti-browning applications can be established.

Supplementary Materials: The following supporting information can be downloaded at https://www.mdpi.com/article/10.3390/md24110382/s1: Table S1, Hydrolysis conditions used for single-enzyme screening and neutral protease–papain ratio optimization; Table S2, Coded and actual levels of independent variables used in the Box–Behnken design; Table S3, Box–Behnken design matrix and experimental results for tyrosinase inhibition; Table S4, Analysis of variance (ANOVA) for the response surface quadratic model of tyrosinase inhibition; Table S5, Acid-hydrolyzable amino acid composition of molecular-weight fractions from golden pompano muscle hydrolysate (mg/g dry weight); Table S6, Apparent Michaelis–Menten parameters of mushroom tyrosinase in the presence of VTPPHVE; Table S7, Concentration–response data for the tyrosinase inhibitory activity of the selected peptides; Table S8, LC–MS/MS identification metrics and protein accession information of the five synthesized peptides; Table S9, Global nonlinear regression analysis of alternative inhibition models for VTPPHVE against mushroom tyrosinase; Figure S1, Annotated MS/MS spectra of the five synthesized peptides identified in the <3 kDa fraction. (A) EEGSPDWRR; (B) LDKPGPPT; (C) VTPPHVE; (D) TPGPTGPIK; and (E) EKLGDLYR.; Figure S2, Concentration–response curves of the synthesized peptides for tyrosinase inhibition. (A) EEGSPDWRR, (B) VTPPHVE, and (C) EKLGDLYR.; Figure S3, Photograph of the golden pompano raw material used in this study.

Author Contributions: N.A.: Investigation, data curation, software, writing—original draft. Y.Z.: Methodology, validation, formal analysis. H.W.: Conceptualization, investigation, writing—review and editing. W.B.: Resources, supervision. H.D.: Writing—review and editing, formal analysis. J.P.: Formal analysis, data curation. Y.X.: Supervision, funding acquisition. J.L.: Project administration, funding acquisition. All authors have read and agreed to the published version of the manuscript.

Funding: This research was supported by the Guangdong Province Key Field R&D Program "Marine Technology" Major Special Flagship Project (2025B1111140001), the National Natural Science Foundation of China (32572493), and the Guangdong Provincial Key Discipline Research Capacity Enhancement Project (2025ZDJS002).

Institutional Review Board Statement: Not applicable.

Data Availability Statement: The original contributions presented in this study are included in the article/Supplementary Material. Further inquiries can be directed to the corresponding author.

Conflicts of Interest: The authors declare no conflicts of interest.

References

1. Li, J.; Feng, L.; Liu, L.; Wang, F.; Ouyang, L.; Zhang, L.; Hu, X.; Wang, G. Recent advances in the design and discovery of synthetic tyrosinase inhibitors. *Eur. J. Med. Chem.* **2021**, *224*, 113744. [CrossRef]
2. Min, X.; Su, Z.; Zhou, H.; Kou, X.; Li, D.; Xu, X. Insights into inhibitory action and interaction of bisdemethoxycurcumin on tyrosinase: Spectroscopic and docking analysis. *Int. J. Biol. Macromol.* **2024**, *281*, 136655. [CrossRef]
3. Liu, L.; Li, J.; Zhang, L.; Wei, S.; Qin, Z.; Liang, D.; Ding, B.; Chen, H.; Song, W. Conformational changes of tyrosinase caused by pentagalloylglucose binding: Implications for inhibitory effect and underlying mechanism. *Food Res. Int.* **2022**, *157*, 111312. [CrossRef]
4. Wang, G.; Zhang, J.; Peng, Z. Tyrosinase inhibitory mechanism of pyrimidine-thiols and their potential application in the anti-browning of fresh-cut apples. *Food Chem.* **2025**, *493*, 146057. [CrossRef]
5. He, M.; Fan, M.; Liu, W.; Li, Y.; Wang, G. Design, synthesis, molecular modeling, and biological evaluation of novel kojic acid derivatives containing bioactive heterocycle moiety as inhibitors of tyrosinase and antibrowning agents. *Food Chem.* **2021**, *362*, 130241. [CrossRef]
6. Kang, M.; Choi, Y.; Byeon, S.-H. Stability, release, and tyrosinase inhibition behaviors of kojic acid encapsulated in the interlayer space of layered yttrium hydroxide. *Appl. Clay Sci.* **2024**, *260*, 107547. [CrossRef]
7. Song, Y.; Chen, S.; Li, L.; Zeng, Y.; Hu, X. The Hypopigmentation Mechanism of Tyrosinase Inhibitory Peptides Derived from Food Proteins: An Overview. *Molecules* **2022**, *27*, 2710. [CrossRef]
8. Ju, X.; Cheng, S.; Li, H.; Xu, X.; Wang, Z.; Du, M. Tyrosinase inhibitory effects of the peptides from fish scale with the metal copper ions chelating ability. *Food Chem.* **2022**, *390*, 133146. [CrossRef]
9. Yap, P.G.; Gan, C.Y. Multifunctional Tyrosinase Inhibitor Peptides with Copper Chelating, UV-Absorption and Antioxidant Activities: Kinetic and Docking Studies. *Foods* **2021**, *10*, 675. [CrossRef]

10. Guo, C.; Yang, X.; Wen, T.; Ma, L.; Zhang, X.; Zhang, M.; Roth, S.; Zhang, M.; Zhang, T. Novel tyrosinase-inhibitory peptides derived from Locusta migratoria protein hydrolysates: Preparation, identification and molecular docking analysis. *Food Chem. X* **2025**, *29*, 102855. [CrossRef]
11. Hou, M.; Xiang, H.; Hu, X.; Chen, S.; Wu, Y.; Xu, J.; Yang, X. Novel potential XOD inhibitory peptides derived from Trachinotus ovatus: Isolation, identification and structure-function analysis. *Food Biosci.* **2022**, *47*, 101639. [CrossRef]
12. Wei, J.; Guo, L.; Liu, J.; Jawad, L.A.; Bouriga, N.; Basyouny Shahin, A.A. Ending the Decades-Long Debate: Trachinotus anak Ogilby, 1909 is the Correct Scientific Name of Golden Pompano in Chinese Aquaculture. *J. Zool. Syst. Evol. Res.* **2026**, *2026*, 2260154. [CrossRef]
13. Mora, L.; Toldrá, F. Advanced enzymatic hydrolysis of food proteins for the production of bioactive peptides. *Curr. Opin. Food Sci.* **2023**, *49*, 100973. [CrossRef]
14. Wan, P.; Cai, B.; Chen, H.; Chen, D.; Zhao, X.; Yuan, H.; Huang, J.; Chen, X.; Luo, L.; Pan, J. Antidiabetic effects of protein hydrolysates from Trachinotus ovatus and identification and screening of peptides with α-amylase and DPP-IV inhibitory activities. *Curr. Res. Food Sci.* **2023**, *6*, 100446. [CrossRef]
15. Ding, X.; Zhao, Y.; Zheng, R.; Cai, J.; Peng, X.; Li, L. Enhanced antioxidant peptide extraction from zein using optimized ultrasound-assisted dual-enzyme methods hydrolysis. *Int. J. Biol. Macromol.* **2025**, *309*, 142938. [CrossRef]
16. Akbarbaglu, Z.; Sarabandi, K.; Peighambardoust, S.H.; Sarabandi, R.; Kafil, H.S.; Hesarinejad, M.A. Enzymatic modification of cold pressed coconut meal protein: Nutritional, functional and biological properties. *Sustain. Food Technol.* **2024**, *2*, 1545–1557. [CrossRef]
17. Qian, J.; Chen, D.; Zhang, Y.; Gao, X.; Xu, L.; Guan, G.; Wang, F. Ultrasound-Assisted Enzymatic Protein Hydrolysis in Food Processing: Mechanism and Parameters. *Foods* **2023**, *12*, 4027. [CrossRef]
18. Guo, L.; Harnedy, P.A.; Li, B.; Hou, H.; Zhang, Z.; Zhao, X.; FitzGerald, R.J. Food protein-derived chelating peptides: Biofunctional ingredients for dietary mineral bioavailability enhancement. *Trends Food Sci. Technol.* **2014**, *37*, 92–105. [CrossRef]
19. Feng, Y.X.; Wang, Z.C.; Chen, J.X.; Li, H.R.; Wang, Y.B.; Ren, D.F.; Lu, J. Separation, identification, and molecular docking of tyrosinase inhibitory peptides from the hydrolysates of defatted walnut (*Juglans regia* L.) meal. *Food Chem.* **2021**, *353*, 129471. [CrossRef]
20. Hu, Z.-Z.; Sha, X.-M.; Zhang, L.; Zha, M.-J.; Tu, Z.-C. From Fish Scale Gelatin to Tyrosinase Inhibitor: A Novel Peptides Screening Approach Application. *Front. Nutr.* **2022**, *9*, 853442. [CrossRef]
21. Yu, Z.; Fu, L.; Zhang, Q.; Zhao, W. In silico identification and molecular mechanism of novel egg white-derived tyrosinase inhibitory peptides. *Food Biosci.* **2024**, *57*, 103567. [CrossRef]
22. Zhao, Y.; Zhang, T.; Ning, Y.; Wang, D.; Li, F.; Fan, Y.; Yao, J.; Ren, G.; Zhang, B. Identification and molecular mechanism of novel tyrosinase inhibitory peptides from the hydrolysate of 'Fengdan' peony (Paeonia ostii) seed meal proteins: Peptidomics and in silico analysis. *LWT* **2023**, *180*, 114695. [CrossRef]
23. Rivero-Pino, F. Bioactive food-derived peptides for functional nutrition: Effect of fortification, processing and storage on peptide stability and bioactivity within food matrices. *Food Chem.* **2023**, *406*, 135046. [CrossRef]
24. Cai, W.-W.; Hu, X.-M.; Wang, Y.-M.; Chi, C.-F.; Wang, B. Bioactive Peptides from Skipjack Tuna Cardiac Arterial Bulbs: Preparation, Identification, Antioxidant Activity, and Stability against Thermal, pH, and Simulated Gastrointestinal Digestion Treatments. *Mar. Drugs* **2022**, *20*, 626. [CrossRef]
25. Chen, Q.; Zhao, Z.; Wang, F.; Chen, T.; Ding, T.; Li, J.; Yao, Z.; Deng, Y.; Wang, Y. Gastrointestinal Fate and Receptor-Mediated Mechanism of GPSGPQGSR, an Intestinal Barrier-Protective Collagen Peptide from ALASKA Pollock Skin. *Mar. Drugs* **2026**, *24*, 203. [CrossRef]
26. Ismaya, W.T.; Rozeboom, H.T.J.; Weijn, A.; Mes, J.J.; Fusetti, F.; Wichers, H.J.; Dijkstra, B.W. Crystal Structure of Agaricus bisporus Mushroom Tyrosinase: Identity of the Tetramer Subunits and Interaction with Tropolone. *Biochemistry* **2011**, *50*, 5477–5486. [CrossRef]
27. Dang, K.; Lan, J.; Wang, Y.; Pan, D.; Du, L.; Suo, S.; Dang, Y.; Gao, X. Screening and evaluation of novel DPP-IV inhibitory peptides in goat milk based on molecular docking and molecular dynamics simulation. *Food Chem. X* **2025**, *25*, 102217. [CrossRef]
28. Wei, G.; Wang, T.; Li, Y.; He, R.; Huang, A.; Wang, X. Identification, structural characterization, and molecular dynamic simulation of ACE inhibitory peptides in whey hydrolysates from Chinese Rushan cheese by-product. *Food Chem. X* **2024**, *21*, 101211. [CrossRef]
29. Zeng, W.; Yu, X.; Chen, M.; Zhang, H.; Xu, J.; Zeng, X.; Liang, Y. ACE-inhibitory peptides from Morchella esculenta: Screening, kinetics, and molecular dynamics simulation. *Food Chem.* **2025**, *490*, 145011. [CrossRef]
30. Yang, B.; Zhong, Z.; Zhang, C.; Jiang, Y.; Zhao, Z.; Wang, X.; Li, Y.; Zheng, H. Identification of novel xanthine oxidase inhibitory peptides from Takifugu obscurus: Peptidomic analysis, molecular docking, and dynamics simulation. *Food Chem.* **2025**, *472*, 142935. [CrossRef]
31. Guo, C.; Wen, T.; Tian, X.; Li, M.; Yu, L.; Zhang, T. Preparation and Mechanistic Characterization of α-Glucosidase Inhibitory Peptides from Elaeagnus mollis Oilseed Meal. *Foods* **2026**, *15*, 1323. [CrossRef]

32. Wang, X.; Fu, J.; Bhullar, K.S.; Chen, B.; Liu, H.; Zhang, Y.; Wang, C.; Liu, C.; Su, D.; Ma, X.; et al. Identification, in silico selection, and mechanistic investigation of antioxidant peptides from corn gluten meal hydrolysate. *Food Chem*. **2024**, *446*, 138777. [CrossRef]
33. Deng, Y.; Huang, L.; Zhang, C.; Xie, P.; Cheng, J.; Wang, X.; Liu, L. Skin-care functions of peptides prepared from Chinese quince seed protein: Sequences analysis, tyrosinase inhibition and molecular docking study. *Ind. Crops Prod*. **2020**, *148*, 112331. [CrossRef]
34. Lin, H.; Zhao, J.; Xie, Y.; Tang, J.; Wang, Q.; Zhao, J.; Xu, M.; Liu, P. Identification and molecular mechanisms of novel antioxidant peptides from fermented broad bean paste: A combined in silico and in vitro study. *Food Chem*. **2024**, *450*, 139297. [CrossRef]
35. Kim, H.H.; Kim, J.K.; Kim, J.; Jung, S.-H.; Lee, K. Characterization of Caffeoylquinic Acids from Lepisorus thunbergianus and Their Melanogenesis Inhibitory Activity. *ACS Omega* **2020**, *5*, 30946–30955. [CrossRef]
36. Ashraf, Z.U.; Gani, A.; Shah, A.; Gani, A.; Punoo, H.A. Ultrasonication assisted enzymatic hydrolysis for generation of pulses protein hydrolysate having antioxidant and ACE-inhibitory activity. *Int. J. Biol. Macromol*. **2024**, *278*, 134647. [CrossRef]
37. Ahmed, T.; Sun, X.; Udenigwe, C.C. Role of structural properties of bioactive peptides in their stability during simulated gastrointestinal digestion: A systematic review. *Trends Food Sci. Technol*. **2022**, *120*, 265–273. [CrossRef]
38. Forli, S.; Huey, R.; Pique, M.E.; Sanner, M.F.; Goodsell, D.S.; Olson, A.J. Computational protein–ligand docking and virtual drug screening with the AutoDock suite. *Nat. Protoc*. **2016**, *11*, 905–919. [CrossRef]
39. Eberhardt, J.; Santos-Martins, D.; Tillack, A.F.; Forli, S. AutoDock Vina 1.2.0: New Docking Methods, Expanded Force Field, and Python Bindings. *J. Chem. Inf. Model*. **2021**, *61*, 3891–3898. [CrossRef]

Disclaimer/Publisher's Note: The statements, opinions and data contained in all publications are solely those of the individual author(s) and contributor(s) and not of MDPI and/or the editor(s). MDPI and/or the editor(s) disclaim responsibility for any injury to people or property resulting from any ideas, methods, instructions or products referred to in the content.